International Communications in Heat and Mass Transfer 167 (2025) 109195

Contents lists available at ScienceDirect

International Communications in Heat and Mass Transfer

journal homepage: www.elsevier.com/locate/ichmt

Simulation of dendritic growth on a spherical surface using a multi-component phase-field model

Sangkwon Kim, Soobin Kwak, Seokjun Ham, Youngjin Hwang, Junseok Kim *

Department of Mathematics, Korea University, Seoul 02841, Republic of Korea

ARTICLE INFO

Keywords:
Dendritic growth
Triangular grid
Computer simulation

ABSTRACT

We consider a numerical algorithm for a phase-field mathematical model of multiple dendritic growth on a spherical surface. One numerical method for curved surfaces is a triangular mesh-based computation method for surfaces. Calculating the governing equations with anisotropic properties using interface angles in a triangular grid is a significant challenge. To solve this issue, we compute the phase-field equation by rotating the triangular mesh relative to the vertex of the crystal seed and then projecting and interpolating it to Cartesian coordinates. When projecting the triangular mesh onto Cartesian coordinates, we apply an adaptive block region that embeds each dendritic phase. The growth simulations of multiple crystals present additional challenges. For multi-crystals, the criteria for rotation are ambiguous; hence, the criteria for rotation are clarified by applying the vector-valued phase-field equation to resolve this problem. Various numerical experiments are conducted on a spherical surface to verify the reliability and robustness of the proposed numerical algorithm to solve the phase-field equations of multiple dendritic growth. We comprehensively present the computational results, and show compelling evidence that validates the reliability and robustness of our computational method.

1. Introduction

Dendritic growth models are employed to simulate the microstructure that solidifies during the casting process. As solidification defects from casting influence subsequent processes and elevate operational costs, it is essential to regulate and forecast the solidifying microstructure. This helps in minimizing defects and, consequently, in cost reduction. Understanding dendritic growth is important because the solidifying microstructure is primarily formed through dendrite growth [1–3].

The phase-field model is based on the concept of an order parameter. The order parameter serves as a numerical descriptor that defines the state or phase of each point within a system and is taken as distinct values in individual phases. For example, in a binary system, the order parameter might assume a value of 0 in one phase and 1 in another. Between these phases, there exists a transition area where the order parameter changes continuously, which effectively describes the diffuse interface. Therefore, it enables the computation of interface movement without tracking the interface. Based on this foundation, the phase-field approach encompasses phenomena from solidification, where it can model the formation of crystals in liquids, to solid-state phase transformations, wherein it can depict changes within the solid phase itself. The phase-field method has been applied to model crystal growth, which effectively simulates the formation of complex dendrites [4–6]. Following this, research on dendritic growth computations based on the phase-field model has attracted increasing attention. Recent studies have applied phase-field simulations to ice crystal growth in NaCl solutions and have studied factors such as subcooling, salt diffusion, and external magnetic fields [7,8]. These works highlight the role of multi-field coupling in accurately predicting dendritic structures and improving desalination efficiency [9]. Laxmipathy et al. [10] performed numerical simulations for the macrostructural evolution of unidirectionally solidified dendrites with different crystal orientations using a multi-component vector-valued phase-field model to study the growth competition of columnar dendrites under convective conditions. Geng et al. [11] introduced an anisotropic interfacial energy function to propose a lattice Boltzmann-phase field model for studying faceted crystal growth. Their study explained the mechanism of faceted structure formation and the evolution of interfacial velocity. Zhao et al. [12] developed surrogate models for computationally efficient phase-field simulations of dendritic microstructures during the solidification process. Fig. 1 presents a snapshot of the freezing of soap bubbles [13].

---

* Corresponding author.
E-mail address: cfdkim@korea.ac.kr (J. Kim).
URL: https://mathematicians.korea.ac.kr/cfdkim/ (J. Kim).

https://doi.org/10.1016/j.icheatmasstransfer.2025.109195

Fig. 1. Freezing of a bubble stacked on an icy substrate. *Source:* Reprinted from Ahmadi et al. [13] with permission from NPG.

First, we consider the following governing equation [14–18]:

$$\mathcal{F} = \int \left[\frac{\epsilon^2(\theta)}{2}|\nabla\phi|^2 + 2\phi^2(1-\phi)^2 + 16\lambda U\left(\frac{\phi^3}{3} - \frac{\phi^4}{2} + \frac{\phi^5}{5}\right)\right] d\mathbf{x}, \tag{1}$$

where ϕ is the phase-field function, and

$$\epsilon(\theta) = \epsilon_0(1 + \epsilon_6\cos(6\theta)). \tag{2}$$

Hence, we have

$$\epsilon^2(\theta)\phi_t = -\frac{\delta\mathcal{F}}{\delta\phi}, \tag{3}$$

where $\frac{\delta\mathcal{F}}{\delta\phi}$ is the variational derivative with respect to ϕ. Then, Eq. (3) can be written as

$$\begin{aligned} \epsilon^2(\theta)\phi_t &= \nabla\cdot(\epsilon^2(\theta)\nabla\phi) + 4[\phi - 0.5 - 2\lambda U\phi(1-\phi)]\phi(1-\phi) \\ &\quad + \left(|\nabla\phi|^2\epsilon(\theta)\frac{\partial\epsilon(\theta)}{\partial\phi_x}\right)_x + \left(|\nabla\phi|^2\epsilon(\theta)\frac{\partial\epsilon(\theta)}{\partial\phi_y}\right)_y, \qquad (4) \\ U_t &= D\Delta U + K\phi_t. \qquad (5) \end{aligned}$$

Here, the subscripts $(\cdot)_t$, $(\cdot)_x$, and $(\cdot)_y$ represent partial differentiation with respect to t, x, and y, respectively

The proposed method rotates all points on the sphere with respect to the crystal center point and then computes ϕ for the rotated points. In contrast, the previous method [19] sets every point on the sphere as a reference and individually rotates its one-ring neighboring points to compute ϕ at the reference point. Fig. 2 schematically illustrates the results of rotating a crystal and projecting it onto the xy-plane using both the proposed (red dash line) and previous (blue solid line) methods. As shown in Fig. 2(b), the previous method leads to mismatches because the rotation axis ($\mathbf{a_r}$ in Eq. (9)) varies depending on the position of the reference point. As a result, different rotation angles (ρ in Eq. (10)) are produced when each point is rotated individually. The primary objective of this study is to resolve this mismatch problem, we propose the method that rotates all points based on a single reference point, guaranteeing consistency in the rotation process.

After rotation and interpolation, standard finite difference methods are applied to solve Eq. (4) numerically. Then, we subsequently interpolate and project the numerical solution of Eq. (4) back to the triangular mesh. Next, we solve Eq. (5) on a triangular mesh using the Laplace–Beltrami operator (LBO).

However, we encountered an additional problem in the simulation of the growth of multiple crystals. If there are multiple crystals, the reference for rotation is ambiguous. Hence, to resolve this problem, we applied a vector-valued phase-field equation. A 2D phase-field equation for multiple dendritic growth is as follows:

$$\begin{aligned} \epsilon^2(\theta_k)(\phi_k)_t &= \nabla\cdot(\epsilon^2(\theta_k)\nabla\phi_k) + 4[\phi_k - 0.5 - 2\lambda U\phi_k(1-\phi_k)]\phi_k(1-\phi_k) \\ &\quad + \left(|\nabla\phi_k|^2\epsilon(\theta_k)\frac{\partial\epsilon(\theta_k)}{\partial(\phi_k)_x}\right)_x + \left(|\nabla\phi_k|^2\epsilon(\theta_k)\frac{\partial\epsilon(\theta_k)}{\partial(\phi_k)_y}\right)_y, \qquad (6) \\ U_t &= D\Delta U + K\sum_{k=1}^{N}(\phi_k)_t, \qquad (7) \end{aligned}$$

where k denotes kth component of crystal for $k = 1,\ldots,N$, ϕ_k and θ_k are the vector-valued phase-field and angle of the k-th crystal, respectively. Here, θ_k is the angle between the normal vector, $-\nabla\phi_k = (-(\phi_k)_x, -(\phi_k)_y)$, of the interface and the x-axis, i.e., $\theta_k = \tan^{-1}\left((\phi_k)_y/(\phi_k)_x\right)$. The anisotropic term is $\epsilon(\theta_k) = \epsilon_0(1+\epsilon_6\cos(6\theta_k))$. Let

$$\begin{aligned} \left(|\nabla\phi_k|^2\epsilon(\theta_k)\frac{\partial\epsilon(\theta_k)}{\partial(\phi_k)_x}\right)_x &= \left(((\phi_k)_x^2+(\phi_k)_y^2)\epsilon(\theta_k)\epsilon'(\theta_k)\left(-\frac{(\phi_k)_y}{(\phi_k)_x^2+(\phi_k)_y^2}\right)\right)_x \\ &= -\left(\epsilon'(\theta_k)\epsilon(\theta_k)(\phi_k)_y\right)_x, \\ \left(|\nabla\phi_k|^2\epsilon(\theta_k)\frac{\partial\epsilon(\theta_k)}{\partial(\phi_k)_y}\right)_y &= \left(((\phi_k)_x^2+(\phi_k)_y^2)\epsilon(\theta_k)\epsilon'(\theta_k)\frac{(\phi_k)_x}{(\phi_k)_x^2+(\phi_k)_y^2}\right)_y \\ &= \left(\epsilon'(\theta_k)\epsilon(\theta_k)(\phi_k)_x\right)_y. \end{aligned}$$

Therefore, Eq. (6) can be rewritten as

$$\begin{aligned} \epsilon^2(\theta_k)\frac{\partial\phi_k}{\partial t} &= \nabla\cdot(\epsilon^2(\theta_k)\nabla\phi_k) + 4[\phi_k - 0.5 - 2\lambda U\phi_k(1-\phi_k)]\phi_k(1-\phi_k) \\ &\quad - \left(\epsilon'(\theta_k)\epsilon(\theta_k)(\phi_k)_y\right)_x + \left(\epsilon'(\theta_k)\epsilon(\theta_k)(\phi_k)_x\right)_y. \end{aligned} \tag{8}$$

The rest of this paper is structured as follows. In Section 2, we describe the computational method in detail. In Section 3, we present many numerical experiments. Section 4 provides a summary of conclusions.

2. Computational method

In this section, we describe the computational algorithm for solving the two-dimensional phase-field Eq. (7) and (8) on a spherical surface. For anisotropic dendritic growth, we first rotate the spherical surface in three-dimensional (3D) space, with radius R, so that the crystal seed is located at the North Pole point. Then, we project the spherical surface onto a two-dimensional plane to solve Eq. (8). On the other hand, since Eq. (7) assumes isotropic behavior, it is solved directly on the spherical surface in 3D space. To avoid confusion, we denote points on the spherical surface in 3D space by (x, y, z), and points in the projected two-dimensional plane for anisotropic dendritic growth by (X, Y). The detailed description of the numerical algorithm is presented in the remainder of this section.

Let a spherical surface $\mathcal{S}$ of radius R be centered at $(x,y,z) = (0,0,0)$. We generate a triangular mesh $\mathcal{S}^d$ using the SphereMesh function in MATLAB [20]. We will rotate the spherical surface $\mathcal{S}$ so that the coordinate of the vertex of the crystal center (seed) point $\mathbf{x}_c$ is the North Pole point $\mathbf{x}_t = (0,0,R)$. To rotate the spherical surface, let us define the rotation axis $\mathbf{a_r}$ as follows

$$\mathbf{a_r} = \frac{\mathbf{x}_c\times\mathbf{x}_t}{|\mathbf{x}_c\times\mathbf{x}_t|}, \tag{9}$$

as shown in Fig. 3(a). Once the axis of rotation $\mathbf{a_r}$ is determined, the angle of rotation φ, which represents the amount of rotation, is defined as the angle between the two vectors $\mathbf{x}_c$ and $\mathbf{x}_t$, i.e.,

$$\varphi = \cos^{-1}\left(\frac{\mathbf{x}_c\cdot\mathbf{x}_t}{|\mathbf{x}_c||\mathbf{x}_t|}\right). \tag{10}$$

To locate the crystal seed $\mathbf{x}_c$ to $\mathbf{x}_t$, We rotate the spherical surface $\mathcal{S}^d$ around $\mathbf{a_r}$ by φ [21]:

$$\tilde{\mathbf{x}}_s = (1-\cos(\varphi))(\mathbf{x}_s\cdot\mathbf{a_r})\mathbf{a_r} + \cos(\varphi)\mathbf{x}_s + \sin(\varphi)\mathbf{a_r}\times\mathbf{x}_s, \quad \text{for } \forall\mathbf{x}_s\in\mathcal{S}^d. \tag{11}$$

Next, to reduce the computational cost, we define sub-domain $\tilde{\mathcal{S}}'$ including the crystal and belonging to the upper spherical cap, see Fig. 3(b). We compute ϕ not in the entire domain $\mathcal{S}$, but in the upper spherical cap $\tilde{\mathcal{S}}'$. Herein, $\theta_h(\in(0,\pi/2))$ of the cap is the polar angle between the rotated crystal center point $\tilde{\mathbf{x}}_c(=(0,0,R))$ and the edge of the disc forming the base of the cap. This angle is determined according to the size of the crystal to ensure that the spherical cap encompasses the crystal. Specifically, it is always greater than the polar angle θ_p between the rotated crystal center point and the crystal tip. We used

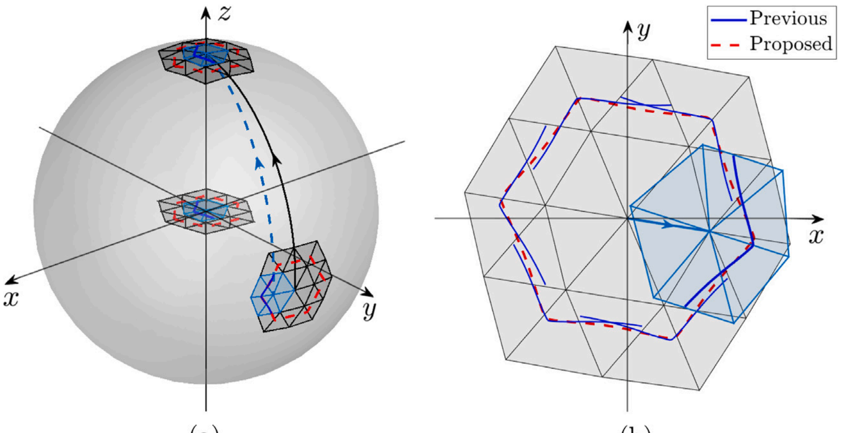

(a) (b)

Fig. 2. Schematic diagram for the previous and proposed rotation methods.

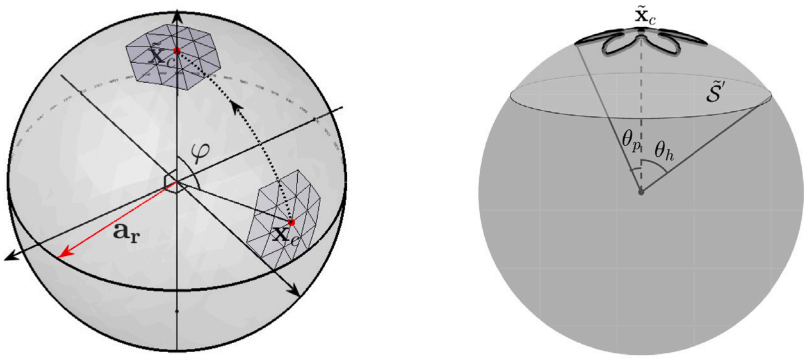

(a) (b)

Fig. 3. Schematic for rotation algorithm and the computational domain for ϕ.

$\theta_h = \theta_p + \pi/36$. In Fig. 5, the region represented in light green indicates the sub-domain $\tilde{S}'$, which is adaptively determined based on the size of the crystal.

The points $\tilde{\mathbf{x}}_s (\in \tilde{S}')$ are projected onto the xy-plane, which we denote it as $\hat{\mathbf{x}}_s$. Next, the projected points $\hat{\mathbf{x}}_s$ are extended by accounting for the arc length between each $\tilde{\mathbf{x}}_s$ and the rotated crystal center $\tilde{\mathbf{x}}_c$, as follows:

$$\bar{\mathbf{x}}_s = R\cos^{-1}\left(\frac{\tilde{\mathbf{x}}_s\cdot\tilde{\mathbf{x}}_c}{|\tilde{\mathbf{x}}_s||\tilde{\mathbf{x}}_c|}\right)\frac{\hat{\mathbf{x}}_s}{|\hat{\mathbf{x}}_s|}. \tag{12}$$

Finally, we interpolate the phase-field values and the temperature field values from the projected values at the vertices $\bar{\mathbf{x}}_s$ using the scatteredInterpolant function in MATLAB [22].

We solve now Eq. (6) using values interpolated into the two-dimensional Cartesian local coordinate. Let h be grid size, $N = [2L/h]+1$ be the number of grids with $L = \theta_h R$, and $\Omega^d = \{X_i = -L + (i-0.5)h,\ Y_j = -L + (j-0.5)h,\ 1 \le i,j \le N\}$ be the set of cell centers. Let $\phi^n_{k,ij} = \phi_k(X_i, Y_j, n\Delta t)$, $U^n_{ij} = U(X_i, Y_j, n\Delta t)$, and $\theta^n_{k,ij} = \theta_k(X_i, Y_j, n\Delta t)$). Then, Eq. (8) is discretized as follows:

$$\begin{aligned}\epsilon^2(\theta^n_{k,ij})\frac{\phi^{n+1}_{k,ij}-\phi^n_{k,ij}}{\Delta t} &= \left[\nabla_d\cdot(\epsilon^2(\theta_k)\nabla_d\phi_k)\right]^n_{ij}\\ &\quad+4[\phi^n_{k,ij}-0.5-2\lambda U^n_{ij}\phi^n_{k,ij}(1-\phi^n_{k,ij})]\phi^n_{k,ij}(1-\phi^n_{k,ij})\\ &\quad-\left[D_x\left(\epsilon'(\theta_k)\epsilon(\theta_k)D_y\phi_k\right)\right]^n_{ij}+\left[D_y\left(\epsilon'(\theta_k)\epsilon(\theta_k)D_x\phi_k\right)\right]^n_{ij},\end{aligned} \tag{13}$$

where $\theta^n_{k,ij}$ is the angle at $\bar{\mathbf{x}}^n_{ij}$, and $\nabla_d\phi_k = (D_x\phi_k,\ D_y\phi_k)$ is the discrete gradient. The two terms in Eq. (14) are

$$\epsilon(\theta^n_{k,ij}) = \epsilon_0\left(1+\epsilon_6\cos(6(\theta^n_{k,ij}-\bar{\theta}))\right), \tag{14}$$

$$\epsilon'(\theta^n_{k,ij}) = -6\epsilon_0\epsilon_6\sin(6(\theta^n_{k,ij}-\bar{\theta})), \tag{15}$$

where $\bar{\theta}$ is an orientation angle. To compute $\epsilon^2(\theta^n_{k,ij})$, we define

$$-\nabla_d\phi^n_{k,ij} = -(D_x\phi^n_{k,ij},\ D_y\phi^n_{k,ij}) = -\left(\frac{\phi^n_{k,i+1,j}-\phi^n_{k,i-1,j}}{2h},\ \frac{\phi^n_{k,i,j+1}-\phi^n_{k,i,j-1}}{2h}\right).$$

Hence, we have

$$\theta^n_{k,ij} = \tan^{-1}\left(\frac{\phi^n_{k,i,j-1}-\phi^n_{k,i,j+1}}{\phi^n_{k,i-1,j}-\phi^n_{k,i+1,j}}\right). \tag{16}$$

Using this angle $\theta^n_{k,ij}$ and Eq. (14), we compute $\epsilon^2(\theta^n_{k,ij})$. Next, we get

$$\begin{aligned}&\left[\nabla_d\cdot(\epsilon^2(\theta_k)\nabla_d\phi_k)\right]^n_{ij}\\ &\quad=\frac{\epsilon^2(\theta^n_{k,i+\frac{1}{2},j})\left(\phi^n_{k,i+1,j}-\phi^n_{k,ij}\right)-\epsilon^2(\theta^n_{k,i-\frac{1}{2},j})\left(\phi^n_{k,ij}-\phi^n_{k,i-1,j}\right)}{h^2}\\ &\quad+\frac{\epsilon^2(\theta^n_{k,i,j+\frac{1}{2}})\left(\phi^n_{k,ij}-\phi^n_{k,i,j+1}\right)-\epsilon^2(\theta^n_{k,i,j-\frac{1}{2}})\left(\phi^n_{k,ij}-\phi^n_{k,i,j-1}\right)}{h^2},\\ &\left[D_x\left(\epsilon'(\theta_k)\epsilon(\theta_k)D_y\phi_k\right)\right]^n_{ij}\\ &\quad=\frac{\epsilon'(\theta_{k,i+\frac{1}{2},j})\epsilon(\theta_{k,i+\frac{1}{2},j})\left(\phi^n_{k,i+1,j+1}-\phi^n_{k,i+1,j-1}+\phi^n_{k,i,j+1}-\phi^n_{k,i,j-1}\right)}{4h^2}\\ &\quad-\frac{\epsilon'(\theta_{k,i-\frac{1}{2},j})\epsilon(\theta_{k,i-\frac{1}{2},j})\left(\phi^n_{k,i,j+1}-\phi^n_{k,i,j-1}+\phi^n_{k,i-1,j+1}-\phi^n_{k,i-1,j-1}\right)}{4h^2},\\ &\left[D_y\left(\epsilon'(\theta_k)\epsilon(\theta_k)D_x\phi_k\right)\right]^n_{ij}\\ &\quad=\frac{\epsilon'(\theta_{k,i,j+\frac{1}{2}})\epsilon(\theta_{k,i,j+\frac{1}{2}})\left(\phi^n_{k,i+1,j+1}-\phi^n_{k,i-1,j+1}+\phi^n_{k,i+1,j}-\phi^n_{k,i-1,j}\right)}{4h^2}\end{aligned}$$

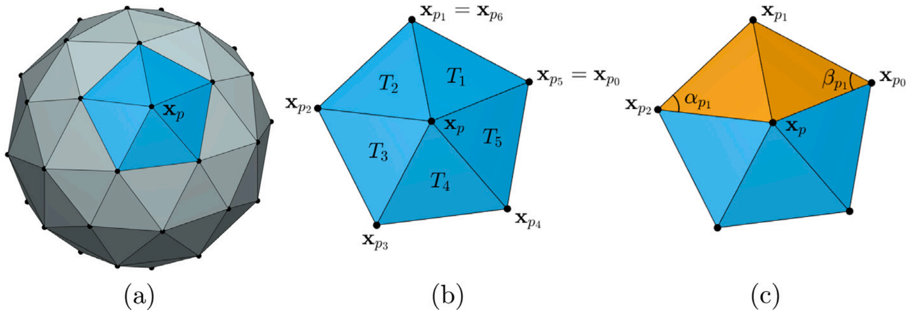

Fig. 4. Schematic illustration of surface mesh.

$$-\frac{\epsilon'(\theta_{k,i,j-\frac{1}{2}})\epsilon(\theta_{k,i,j-\frac{1}{2}})\left(\phi^n_{k,i+1,j} - \phi^n_{k,i-1,j} + \phi^n_{k,i+1,j-1} - \phi^n_{k,i-1,j-1}\right)}{4h^2},$$

where

$$\theta_{k,i-\frac{1}{2},j} = \tan^{-1}\left(\frac{\phi^n_{k,i+1,j-1} - \phi^n_{k,i+1,j+1} + \phi^n_{k,i,j-1} - \phi^n_{k,i,j+1}}{4(\phi^n_{k,ij} - \phi^n_{k,i+1,j})}\right),$$

$$\theta_{k,i+\frac{1}{2},j} = \tan^{-1}\left(\frac{\phi^n_{k,i,j-1} - \phi^n_{k,i,j+1} + \phi^n_{k,i-1,j-1} - \phi^n_{k,i-1,j+1}}{4(\phi^n_{k,i-1,j} - \phi^n_{k,ij})}\right),$$

$$\theta_{k,i,j-\frac{1}{2}} = \tan^{-1}\left(\frac{4(\phi^n_{k,ij} - \phi^n_{k,i,j+1})}{\phi^n_{k,i-1,j+1} - \phi^n_{k,i+1,j+1} + \phi^n_{k,i-1,j} - \phi^n_{k,i+1,j}}\right),$$

$$\theta_{k,i,j+\frac{1}{2}} = \tan^{-1}\left(\frac{4(\phi^n_{k,i,j-1} - \phi^n_{k,ij})}{\phi^n_{k,i-1,j} - \phi^n_{k,i+1,j} + \phi^n_{k,i-1,j-1} - \phi^n_{k,i+1,j-1}}\right).$$

Now, we present a discretization of the LBO [23,24] on the curved surfaces. Fig. 4(a) shows the triangular surface mesh of given spherical surface $\mathcal{S}$. Let n be the number of the one-ring points neighboring $\mathbf{x}_s$ and let $\mathbf{x}_{s_i}$ for $i = 1, 2, \ldots, n$ be the one-ring points neighboring $\mathbf{x}_s$. We define the triangle T_i for $i = 1, 2, \ldots, n$ as $\triangle\, \mathbf{x}_s\mathbf{x}_{s_i}\mathbf{x}_{s_{i-1}}$ and define the angles α_{s_i} and β_{s_i} as $\angle \mathbf{x}_s\mathbf{x}_{s_{i+1}}\mathbf{x}_{s_i}$ and $\angle \mathbf{x}_s\mathbf{x}_{s_{i-1}}\mathbf{x}_{s_i}$, respectively, where $\mathbf{x}_{s_0} = \mathbf{x}_{s_n}$ and $\mathbf{x}_{s_{n+1}} = \mathbf{x}_{s_1}$. The area of the triangle T_i is defined by

$$a(T_i) = \frac{1}{2}\sqrt{|\mathbf{x}_{s_i} - \mathbf{x}_s|^2|\mathbf{x}_{s_{i-1}} - \mathbf{x}_s|^2 - \left(\mathbf{x}_{s_i} - \mathbf{x}_s, \mathbf{x}_{s_{i-1}} - \mathbf{x}_s\right)^2}$$

and the sum of the area of the triangles is defined by

$$A(\mathbf{x}_s) = \sum_{i=1}^{n} a(T_i).$$

Then, the discrete LBO at $\mathbf{x}_s$ [25] is given by

$$\Delta_{\mathcal{S}} U_s \approx \frac{3}{A(\mathbf{x}_s)}\sum_{i=1}^{n}\frac{\cot\alpha_{s_i} + \cot\beta_{s_i}}{2}(U_{s_i} - U_s),$$

where $U_s = U(\mathbf{x}_s)$ and $U_{s_i} = U(\mathbf{x}_{s_i})$.

3. Computational tests

We use $R = 120$, the number of crystal seeds $N = 1$, and the initial angle of the spherical cap $\theta_h = \pi/18 = 10°$. Here, if the distance between the tip of the crystal and the edge of the disc forming the base of the cap is less than any reference, increase the angle θ_h of the cap by $\pi/36 = 5°$ to widen the computational domain. We use the default values of parameters: $\lambda = 3.1913$, $\epsilon_0 = 1$, $\epsilon_6 = 1/(6^2 - 1)$, $\bar{\theta} = \pi/6$, $D = 1$, $h = 0.5$, and $\Delta t = 0.1h^2/D$.

3.1. Temporal evolution

To consider isothermal crystallization on spheres. we use the following initial conditions:

$$\phi(\mathbf{x}_s, 0) = \frac{1}{2}\left(1 + \tanh\left(\frac{r - R\theta}{\sqrt{2}}\right)\right), \tag{17}$$

$$U(\mathbf{x}_s, 0) = \left(1 - \phi(\mathbf{x}_s, 0)\right)\Delta,$$

where $\theta = \cos^{-1}\left((\mathbf{x}_s) \cdot (0, 0, R)\right)$, undercooling $\Delta = -0.65$, and $r = 5$ for $\mathbf{x}_s = (x_s, y_s, z_s) \in \mathcal{S}^d$. Fig. 5 shows snapshots of the anisotropic ice crystal growth at different times $t = 0\Delta t$, $4000\Delta t$, $8000\Delta t$, and $12000\Delta t$. The computational domain is shown in fluorescent colors and as the crystals grew, the computational domain expands.

3.2. Effect of the simulation parameters

We conducted the comparison test on the evolution of crystal growth depending on the simulation parameters such as orientation angle $\bar{\theta}$, latent heat K, and the curvature $2/R$ at $t = 6000\Delta t$. Fig. 6 corresponds to the results for the orientation angle, thermal parameter, and spherical radius, respectively. Each row presents the results for a specific test parameter, while each column, from left to right, represents simulations conducted with different values of the corresponding parameter.

First, Fig. 6(a) shows the results for different orientation angles, $\bar{\theta} = 2\pi/12, 3\pi/12$, and $4\pi/12$. Regardless of the orientation angle, the dendritic structures crystallize effectively, which indicates that the proposed method can stably simulate anisotropic crystal growth for different preferred orientations. The overall morphology remains consistent while adapting to the specified angular alignment.

Second, Fig. 6(b) presents the results for different latent heat values, $K = 0.9, 1.0$, and 1.1. The latent heat parameter influences the branching structure of the dendrites, where higher K values result in more pronounced and well-developed branches. Conversely, when K is lower, the branching becomes less prominent, and the dendritic shape becomes more compact. Based on this test, $K = 1.0$ is chosen for all subsequent simulations as it provides a balanced branching structure suitable for studying dendritic growth dynamics.

Last, Fig. 6(c) shows the results of the proposed scheme for different spherical radii, $R = 90$,120, and 150. Note that for a smaller spherical radius (higher curvature), the dendrites appear less ramified. Based on this test, $R = 120$ is chosen for all subsequent simulations.

3.3. Effect of position of crystal

We compare the evolution of the crystal growth according to the initial position on spherical domain. Fig. 7 schematically illustrates the process of rotating and projecting two crystals located at different positions using the proposed method. Fig. 7(a) presents the two crystals, while Fig. 7(b) and (d) depict the rotation of the sphere based on the center of each crystal. Fig. 7(c) and (e) show the projection of the rotated crystals onto the xy-plane. In Fig. 7(b)–(e), the solid line represents the x-axis, while the dashed line indicates a vector forming an angle equal to the reference angle $\bar{\theta}$ with the x-axis. As observed in Fig. 7, the rotation angle varies depending on the position of the crystal seed. Consequently, when crystals rotated from different positions are projected onto the xy-plane, their reference angles differ. This discrepancy arises because the rotation axis changes with the seed position, which causes the sphere to rotate around different axes,

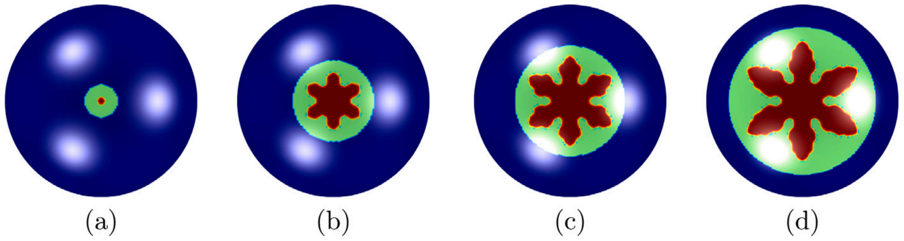

Fig. 5. Evolution of the phase at (a) $t = 0\Delta t$, (b) $t = 4000\Delta t$, (c) $t = 8000\Delta t$, and (d) $t = 12000\Delta t$.

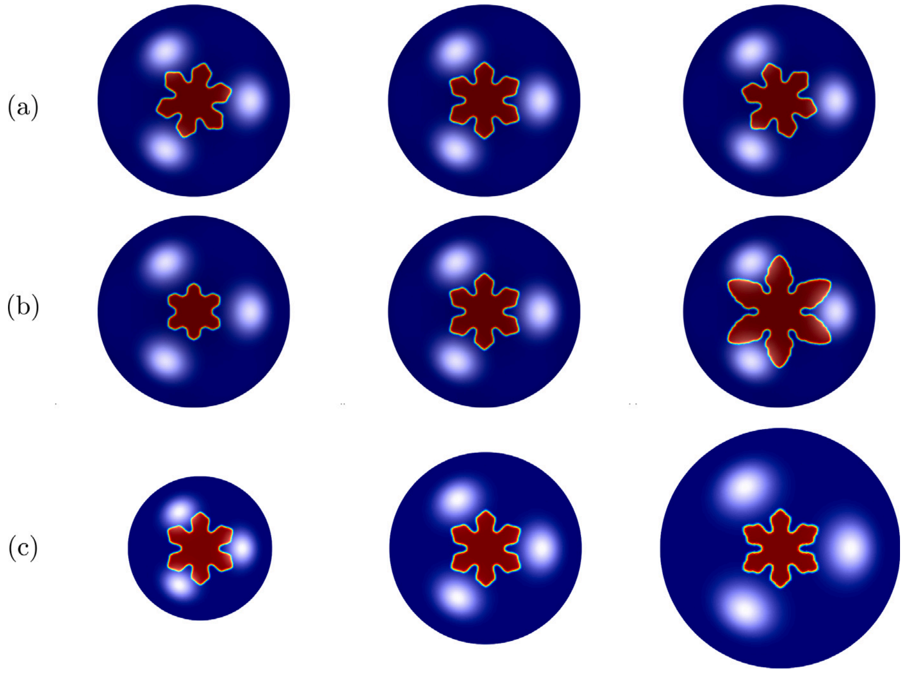

Fig. 6. Dendritic growth with various simulation parameters such as (a) the orientation angle $\bar{\theta} = 2\pi/12$, $\bar{\theta} = 3\pi/12$, and $\bar{\theta} = 4\pi/12$, (b) the latent heat $K = 1.1$, $K = 1.0$, and $K = 0.9$, and (c) the spherical radii $R = 90$, $R = 120$, and $R = 150$ at $t = 6000\Delta t$.

whereas the xy-plane remains fixed and does not rotate. Therefore, the proposed method ensures that the reference angle of polycrystalline is determined according to the rotation angle ρ at each position. This guarantees that all crystals grow while maintaining a consistent reference angle, regardless of the initial position and rotation of the seed.

Given that the proposed method can reliably simulate anisotropic crystal growth for different preferred orientations, it is important to keep in mind that the phase evolution results correspond to different reference angles depending on the position of the crystal. The central position of the crystal follows a spherical coordinate system, and the pairs of poles ψ and azimuth ξ angles of the radiation used $(\psi, \xi) = (0,0), (\pi/5, 0), (2\pi/5, 0), (3\pi/5, 0), (4\pi/5, 0)$, and $(\pi, 0)$. Fig. 8 displays the evolution of crystal growth according to position using the proposed algorithm. As shown in Fig. 8, we see a similar dendrite growth at all positions. Thus, this test demonstrates the robustness of the our scheme to crystal growth according to the position on the sphere.

3.4. Influence between crystals

Interference exists as multiple crystals grow in a limited area. In this section, numerical experiments have been conducted on this situation, and numerical results are presented when there is a time difference in crystal seed production. First, we conducted numerical experiments on the growth of multiple crystals in parallel. To consider multiple isothermal crystallization on spheres, we use the following initial conditions:

$$\phi(\mathbf{x}_s, 0) = \sum_{k=1}^{N} \frac{1}{2} \left(1 + \tanh\left(\frac{r - R\theta_k}{\sqrt{2}} \right) \right), \qquad (18)$$
$$U(\mathbf{x}_s, 0) = \left(1 - \phi(\mathbf{x}_s, 0) \right) \Delta,$$

where $\theta_k = \cos^{-1}(\mathbf{v}_k \cdot \mathbf{x}_s)$. Fig. 9 illustrates the progression of anisotropic multiple crystal growth at different times 0, $3000\Delta t$, $6000\Delta t$, and $10000\Delta t$ from (a) to (d), and highlights the competitive interactions that emerge as the crystals expand. Initially, as shown in Fig. 9(a), several nucleation sites are distributed within the domain. As time progresses, Fig. 9(b) captures the early growth phase, where individual crystals develop isotropically and maintain distinct boundaries. As the growth continues, interactions between adjacent crystals become more pronounced, which is depicted in Fig. 9(c). By the advanced stage, shown in Fig. 9(d), the closely spaced nucleation sites lead to significant competition. As a result, intricate structural evolution occurs. The proposed method effectively captures these competitive growth dynamics and demonstrates that crystal interfaces interact and influence each other's morphology as they expand.

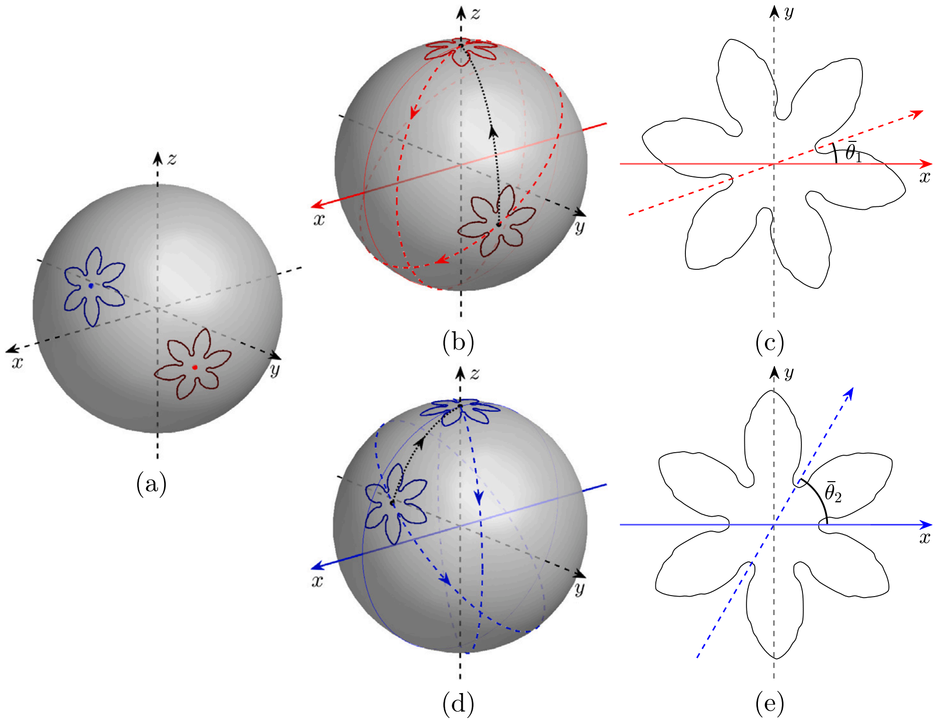

Fig. 7. Schematic of the rotation and projection with $\bar{\theta} = \bar{\theta}_1$, $\bar{\theta}_2$ in the proposed method.

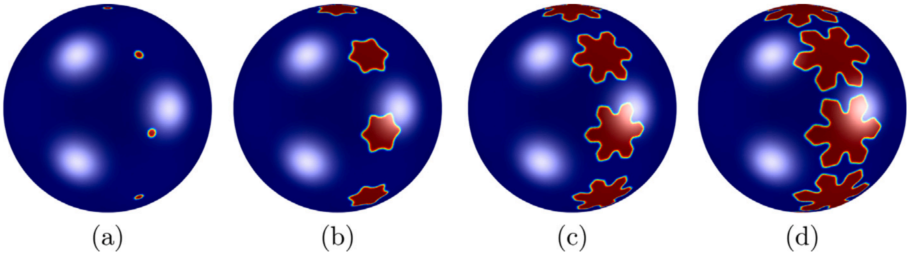

Fig. 8. Evolution of crystal growth by proposed algorithm according to the position of crystal at (a) $t = 0\Delta t$, (b) $t = 2000\Delta t$, (c) $t = 4000\Delta t$, and (d) $t = 6000\Delta t$.

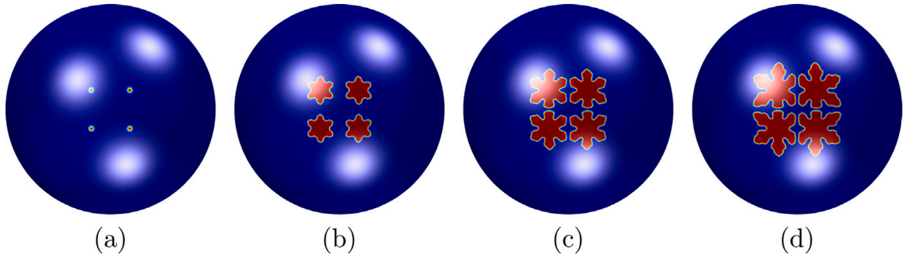

Fig. 9. Snapshot of the multiple crystal growth in parallel at time $t = 0$, $3000\Delta t$, $6000\Delta t$, and $9000\Delta t$ from (a) to (d).

Finally, we performed a numerical simulation for the growth of multiple crystals under conditions where the crystals are generated at different times. In addition, we compare the computational results of our proposed method with those of the previous studies. Therefore, we conducted the test from Section 3.6 in the previous study [19]. Fig. 10 presents snapshots of crystal growth using a level 7 mesh with 20 initial circles, where (a) shows the results of the previous method and (b) presents the outcomes of the proposed method. In Fig. 10(a), some crystals exhibit morphological distortions, which indicates potential inaccuracies in the simulation. In contrast, Fig. 10(b) demonstrates well-preserved crystal shapes, which suggests that the proposed method effectively reduces such distortions. This result demonstrates the robustness of the proposed method in accurately capturing the crystal growth process.

3.5. *k*-fold crystal growth

To explain how the anisotropic term is handled in the governing equation, we conducted numerical simulations for crystal growth with k branches. We defined the anisotropic term by $\epsilon(\phi) = \epsilon_0 \left(1 + \epsilon_k \cos(k\phi)\right)$, where k represents the number of branches in the crystal. This expression directly controls the directional preference of growth and allows

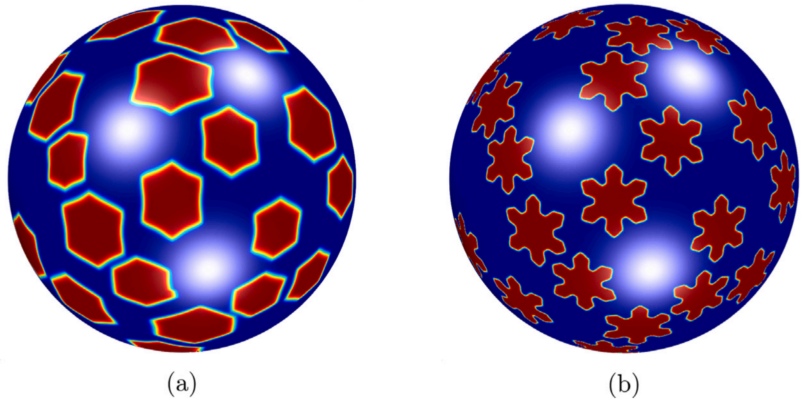
(a) (b)

Fig. 10. Snapshots of crystal growth using a level 7 mesh with 20 initial circles. (a) the result of previous method [19] and (b) the result of the proposed method.

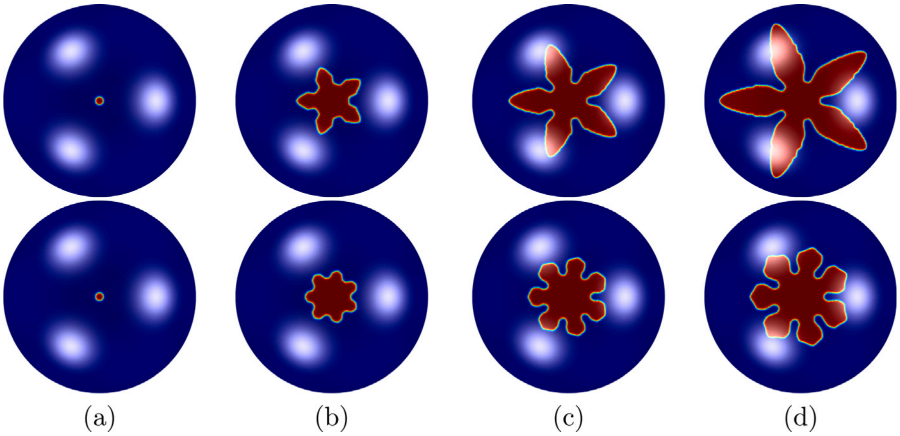
(a) (b) (c) (d)

Fig. 11. Evolution of the phase at (a) $t = 0\Delta t$, (b) $t = 4000\Delta t$, (c) $t = 8000\Delta t$, and (d) $t = 12000\Delta t$. The first row corresponds to $k = 5$ and the second row shows the result for $k = 7$.

the model to simulate k-fold symmetric crystal growth. Therefore, we can perform simulations for several values of k. These simulations confirmed that the model produces distinct k-fold symmetric growth patterns. Fig. 11 shows the results for $k = 5$ and $k = 7$ as representative examples, which demonstrate that the proposed method can naturally reproduce anisotropic morphologies based on the chosen value of k. For the case of $k = 6$, the result is provided in Fig. 5.

3.6. Convergence tests

We conducted a convergence study to assess the accuracy of the proposed algorithm in terms of spatial and temporal resolution. For the spatial test, the time increment was set to $\Delta t = 1.0 \times 10^{-6}$, and computations were performed up to a total time of $15\Delta t$. The initial radius of the crystal and the spherical domain radius were set to $r = 0.25$ and $R = 1$, and the rest of the model parameters were set as described earlier in Section 3.

To evaluate spatial error, we compared the numerical solution obtained at each mesh level with a highly resolved reference solution based on level 8, using the following L^2-norm formula:

$$\|e\| = \sqrt{\frac{1}{M}\sum_{p=1}^{M}(\phi_p - \phi_p^{\mathrm{ref}})^2}. \qquad (19)$$

The variable h denotes the spatial resolution, and the convergence rate was determined from the ratio $\log_2(\|e_h\|/\|e_{h/2}\|)$. The spatial errors and corresponding rates are summarized in Table 1.

We then tested convergence with respect to time. In this case, the mesh was fixed at level 7, which corresponds to $h = 0.007$, and the system evolved until $t = 3.0 \times 10^{-5}$. For error estimation, we used the L^2-norm, Eq. (19), where the reference solution was computed using a fine time step of $\Delta t = 3.125 \times 10^{-8}$. The temporal convergence rate was calculated by taking $\log_2(\|e_{\Delta t}\|/\|e_{\Delta t/2}\|)$. Table 2 provides the temporal error data.

These results indicate that the scheme reaches second-order convergence in space and nearly first-order convergence in time.

Table 1
Spatial convergence test results.

Grid size, h	L^2-Error	Rate
0.028	7.0473×10^{-5}	–
0.014	1.6066×10^{-5}	2.1331
0.007	4.0892×10^{-6}	1.9741

Table 2
Temporal convergence test results.

Time step, Δt	L^2-Error	Rate
1.0×10^{-6}	4.0907×10^{-8}	–
5.0×10^{-7}	1.9699×10^{-8}	1.0543
2.5×10^{-7}	9.1707×10^{-9}	1.1030

4. Conclusions

In this work, we have presented a computational method for the phase-field equation of multiple anisotropic dendritic growth. By using the developed algorithm, we successfully conducted simulations of freezing bubbles. One numerical method for curved surfaces is a triangular mesh-based computation method for surfaces. We solved the governing equation by rotating the triangular mesh relative to the vertex of the crystal seed and then by projecting and interpolating it to Cartesian coordinates. When projecting the triangular mesh into Cartesian coordinates, we apply an adaptive block region that embeds each dendritic phase to get the computational efficiency. This approach became more effective as the number of crystals increased. The vector-valued Allen–Cahn equation was applied to clarify the criterion of rotation in the case of polycrystals. Various numerical tests were conducted on a spherical surface to validate the reliability and robustness of the proposed computational algorithm for solving the phase-field equations of multiple dendritic growth. We thoroughly evaluated the computational results obtained in these tests, and provided strong evidence confirming the reliability and robustness of our computational scheme. In addition, the subject of future research is to simulate the growth of polycrystals and collisions between crystals while the crystals on the spherical surface move in consideration of fluid flow.

CRediT authorship contribution statement

Sangkwon Kim: Writing – original draft, Methodology, Investigation, Formal analysis, Conceptualization. **Soobin Kwak:** Writing – original draft, Validation, Software, Methodology, Investigation, Formal analysis, Data curation, Conceptualization. **Seokjun Ham:** Writing – original draft, Methodology, Investigation, Conceptualization. **Youngjin Hwang:** Writing – original draft, Software, Methodology. **Junseok Kim:** Writing – original draft, Supervision, Software, Resources, Project administration, Investigation, Conceptualization.

Declaration of competing interest

The authors declare that they have no known competing financial interests or personal relationships that could have appeared to influence the work reported in this paper.

Acknowledgments

The first author (S.K. Kim) was supported by the National Research Foundation of Korea(NRF) grant funded by the Korea government(MSIT) (No. 2022R1C1C2005275). The corresponding author (J.S. Kim) was supported by the National Research Foundation of Korea(NRF) grant funded by the Korea government(MSIT) (No. 2022R1A2C1003844). The authors sincerely appreciate the reviewers' insightful comments and constructive suggestions, which have greatly improved the quality of this manuscript.

Data availability

Data will be made available on request.

References

[1] J.S. Langer, Instabilities and pattern formation in crystal growth, Rev. Modern Phys. 52 (1) (1980) 1, http://dx.doi.org/10.1103/RevModPhys.52.1.

[2] T. DebRoy, S.A. David, Physical processes in fusion welding, Rev. Modern Phys. 67 (1) (1995) 85, http://dx.doi.org/10.1103/RevModPhys.67.85.

[3] W.J. Boettinger, S.R. Coriell, A.L. Greer, A. Karma, W. Kurz, M. Rappaz, R. Trivedi, Solidification microstructures: recent developments, future directions, Acta Mater. 48 (1) (2000) 43–70, http://dx.doi.org/10.1016/S1359-6454(99)00287-6.

[4] R. Kobayashi, Modeling and numerical simulations of dendritic crystal growth, Physica D 63 (3–4) (1993) 410–423, http://dx.doi.org/10.1016/0167-2789(93)90120-P.

[5] C. Li, J. Wen, L. Wang, G. Lei, Q. Chen, Modeling of solid-air multi-dendrite growth evolution driven by coupled thermal-solute using non-isothermal quantitative phase field method, Int. J. Heat Mass Transfer 145 (2023) 106841, http://dx.doi.org/10.1016/j.icheatmasstransfer.2023.106841.

[6] C. Li, J. Wen, K. Li, S. Wang, Modeling coupled growth and motion of solid-air dendrite induced by convection in liquid hydrogen using phase-field lattice Boltzmann method, Int. J. Heat Mass Transfer 153 (2024) 107380.

[7] H. Yuan, K. Sun, K. Wang, J. Zhang, Z. Zhang, L. Zhang, S. Li, Y. Li, Ice crystal growth in the freezing desalination process of binary water-NaCl system, Desalination 496 (2020) 114737, http://dx.doi.org/10.1016/j.desal.2020.114737.

[8] R. Song, K. Wang, M. Gong, H. Yuan, Multi-physical field simulations of directional seawater freeze-crystallisation under a magnetic field, Desalination 560 (2023) 116687, http://dx.doi.org/10.1016/j.desal.2023.116687.

[9] D. Leng, P. Li, F. Kong, H. Zhang, T. Yang, M. Tang, C. Tian, Experimental and numerical study on single ice crystal growth of deionized water and 0.9% NaCl solution under static magnetic field, Int. J. Refrig. 168 (2024) 297–306, http://dx.doi.org/10.1016/j.ijrefrig.2024.09.005.

[10] V.P. Laxmipathy, F. Wang, M. Selzer, B. Nestler, A two-dimensional phase-field study on dendritic growth competition under convective conditions, Comput. Mater. Sci. 186 (2021) 109964, http://dx.doi.org/10.1016/j.commatsci.2020.109964.

[11] B. Geng, S. Mao, W. Chen, D. Sun, Numerical modeling of faceted crystal growth using a lattice Boltzmann-phase field model with a new interfacial energy function, Comput. Mater. Sci. 227 (2023) 112273, http://dx.doi.org/10.1016/j.commatsci.2023.112273.

[12] J. Zhao, J. Li, X. Hu, Y. Wang, Y. Chen, F. He, Z. Wang, Z. Zhao, J. Wang, Establishing reduced-order process-structure linkages from phase field simulations of dendritic grain growth during solidification, Comput. Mater. Sci. 214 (2022) 111694.

[13] S.F. Ahmadi, S. Nath, C.M. Kingett, P. Yue, J.B. Boreyko, How soap bubbles freeze, Nat. Commun. 10 (1) (2019) 2531, http://dx.doi.org/10.1038/s41467-019-10021-6.

[14] A. Karma, W.J. Rappel, Quantitative phase-field modeling of dendritic growth in two and three dimensions, Phys. Rev. E 57 (4) (1998) 4323, http://dx.doi.org/10.1103/PhysRevE.57.4323.

[15] A.A. Wheeler, B.T. Murray, R.J. Schaefer, Computation of dendrites using a phase-field model, Physica D 66 (1–2) (1993) 243–262, http://dx.doi.org/10.1016/0167-2789(93)90242-S.

[16] Y. Li, H.G. Lee, J. Kim, A fast, robust, and accurate operator splitting method for phase-field simulations of crystal growth, J. Cryst. Growth 321 (1) (2011) 176–182, http://dx.doi.org/10.1016/j.jcrysgro.2011.02.042.

[17] T.Z. Gong, Y. Chen, D.Z. Li, Y.F. Cao, P.X. Fu, Quantitative comparison of dendritic growth under forced flow between 2D and 3D phase-field simulation, Int. J. Heat Mass Transfer 135 (2019) 262–273, http://dx.doi.org/10.1016/j.ijheatmasstransfer.2019.01.104.

[18] P. Jiang, S. Gao, S. Geng, C. Han, G. Mi, Multi-physics multi-scale simulation of the solidification process in the molten pool during laser welding of aluminum alloys, Int. J. Heat Mass Transfer 161 (2020) 120316, http://dx.doi.org/10.1016/j.ijheatmasstransfer.2020.120316.

[19] C. Lee, S. Yoon, J. Park, H. Kim, Y. Li, D. Jeong, S. Kim, S. Kwak, J. Kim, Phase-field computations of anisotropic ice crystal growth on a spherical surface, Comput. Math. Appl. 125 (2022) 25–33, http://dx.doi.org/10.1016/j.camwa.2022.08.035.

[20] V. Scalera, P. Ansalone, S. Perna, C. Serpico, M. d'Aquino, Numerical solution of the Fokker–Planck equation by spectral collocation and finite-element methods for stochastic magnetization dynamics, IEEE Trans. Magn. 58 (2) (2021) 1–4, http://dx.doi.org/10.1109/TMAG.2021.3084335.

[21] X. Zhong, D. Yu, Y. San Wong, T. Sim, W.F. Lu, K.W.C. Foong, H.L. Cheng, 3D dental biometrics: Alignment and matching of dental casts for human identification, Comput. Ind. 64 (9) (2013) 1355–1370, http://dx.doi.org/10.1016/j.compind.2013.06.005.

[22] B. Chen, B. Pan, Through-thickness strain field measurement using the mirror-assisted multi-view digital image correlation, Mech. Mater. 137 (2019) 103104, http://dx.doi.org/10.1016/j.mechmat.2019.103104.

[23] G. Xu, Discrete Laplace–Beltrami operators and their convergence, Comput. Aided Geom. Design 21 (8) (2004) 767–784, http://dx.doi.org/10.1016/j.cagd.2004.07.007.

[24] Y. Hwang, S. Ham, C. Lee, G. Lee, S. Kang, J. Kim, A simple and efficient numerical method for the Allen–Cahn equation on effective symmetric triangular meshes, Electron. Res. Arch. 31 (8) (2023) 4557–4578, http://dx.doi.org/10.3934/era.2023225.

[25] H. Kim, S. Kang, G. Lee, S. Yoon, J. Kim, Shape transformation on curved surfaces using a phase-field model, Commun. Nonlinear Sci. Numer. Simul. 133 (2024) 107956, http://dx.doi.org/10.1016/j.cnsns.2024.107956.